Supporting Information

Raman Shifts in Electron-Irradiated Monolayer MoS$_2$

William M. Parkin[1‡], Adrian Balan[1‡], Liangbo Liang[2,3‡], Paul Masih Das[1],

Michael Lamparski[2], Carl H. Naylor[1], Julio A. Rodríguez-Manzo[1],

A. T. Charlie Johnson[1], Vincent Meunier[2]*, Marija Drndić[1]*

[1] Department of Physics and Astronomy, University of Pennsylvania, Philadelphia,

Pennsylvania 19104, United States

[2] Department of Physics, Applied Physics and Astronomy, Rensselaer Polytechnic

Institute, Troy, New York 12180, United States

[3] Center for Nanophase Materials Sciences, Oak Ridge National Laboratory, Oak Ridge,

Tennessee 37831, United States

‡These authors have contributed equally.

*Corresponding authors: Marija Drndić, drndic@physics.upenn.edu; Vincent Meunier,

meuniv@rpi.edu.

Table of Contents:

4. **Kinematic Diffraction Intensities of MoS$_2$ as a function of vacancy percentage.**

5. **Raman modes unaffected by deposition of amorphous carbon layer.**

6. **DFT calculations of phonon frequency shifts.**

7. **Electronic band structure of defective MoS$_2$.**

8. **Imaging during irradiation and after exposure to atmosphere.**

9. **DFT calculations of effects of O substitutional impurities and line defects on phonon frequency shifts.**


Section 1: Effects of laser power on Raman peaks of irradiated MoS$_2$.

To make sure the green (532 nm) Raman laser did not change the Raman peaks in defective MoS$_2$, we took two samples that had each been irradiated to ~1% sulfur vacancy and looked at the Raman peaks at various laser powers. Figures SI 1.1 and SI 1.2 show the results for the first sample, and Figures SI 1.3 and SI 1.4 show results for the second sample. We do not start seeing laser-induced changes in the Raman peaks until a laser power of 5 mW, as shown in Figure SI 1.4. At a laser power of 12.5 mW, the sample is destroyed quickly by the laser.

Using this information, we used a laser power of 2 mW with an exposure time of 13 s/point to make the Raman maps presented in Figure 2. We also took Raman spectra just on individual spots, using 0.2 mW laser with > 2000 second exposure. These two methods produced similar results, and are both included in Figure 4.
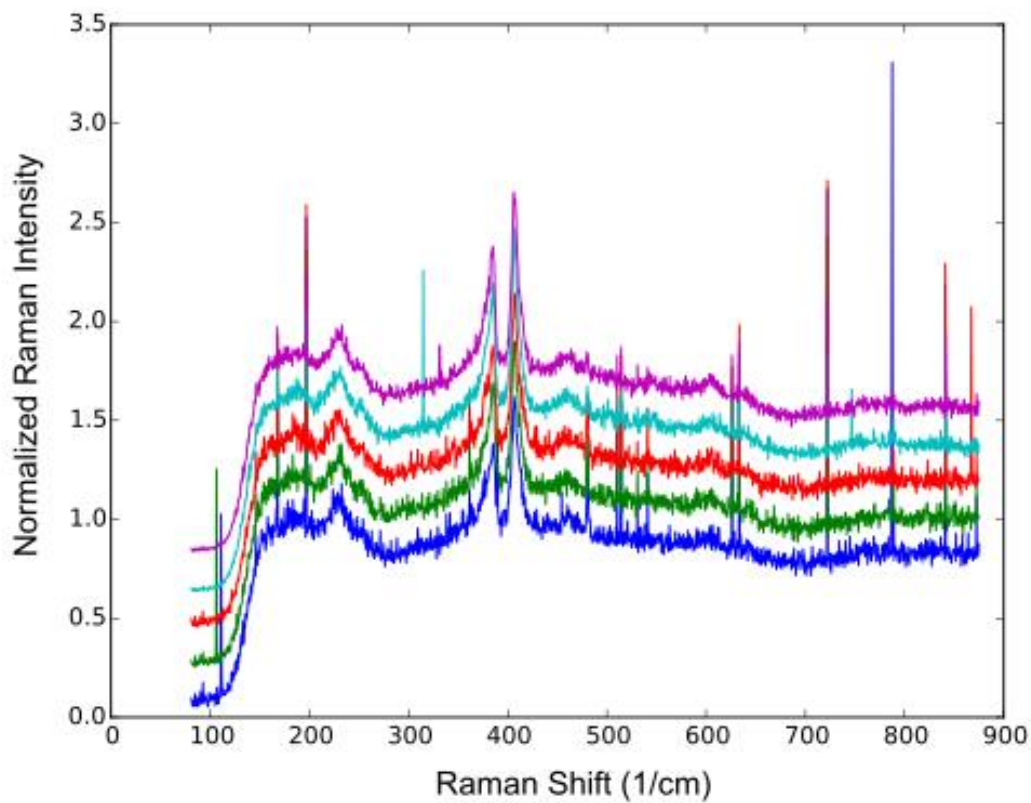
Figure SI 1.1: Raman spectra with increasing laser power. The spectra were shifted vertically for visual clarity. The bottom (blue) trace is the lowest laser power, 0.05 mW. Going up, 0.1 mW (green), 0.1 mW (red), 0.3 mW (cyan), and 0.3 mW (magenta). The exposure times were 7200 s (blue), 4000 s (green), 4000 s (red), 2000 s (cyan), and 2000 s (magenta).
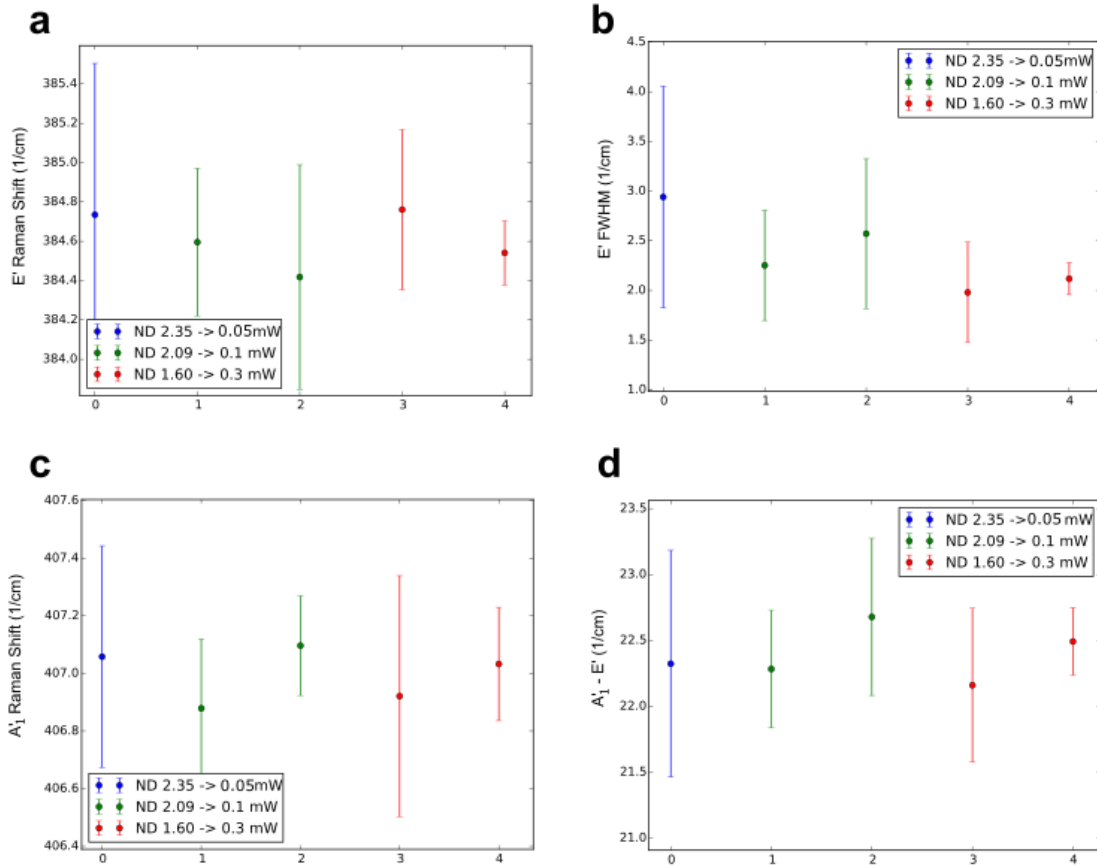
Figure SI 1.2: Peak fits at several laser powers. The spectra in Figure SI 1.1 were fit and peak stats were extracted. a) Location of the E' peak. b) FWHM of the E' peak. c) Location of the A'_1 peak. d) Separation between the E' and A'_1 peaks.
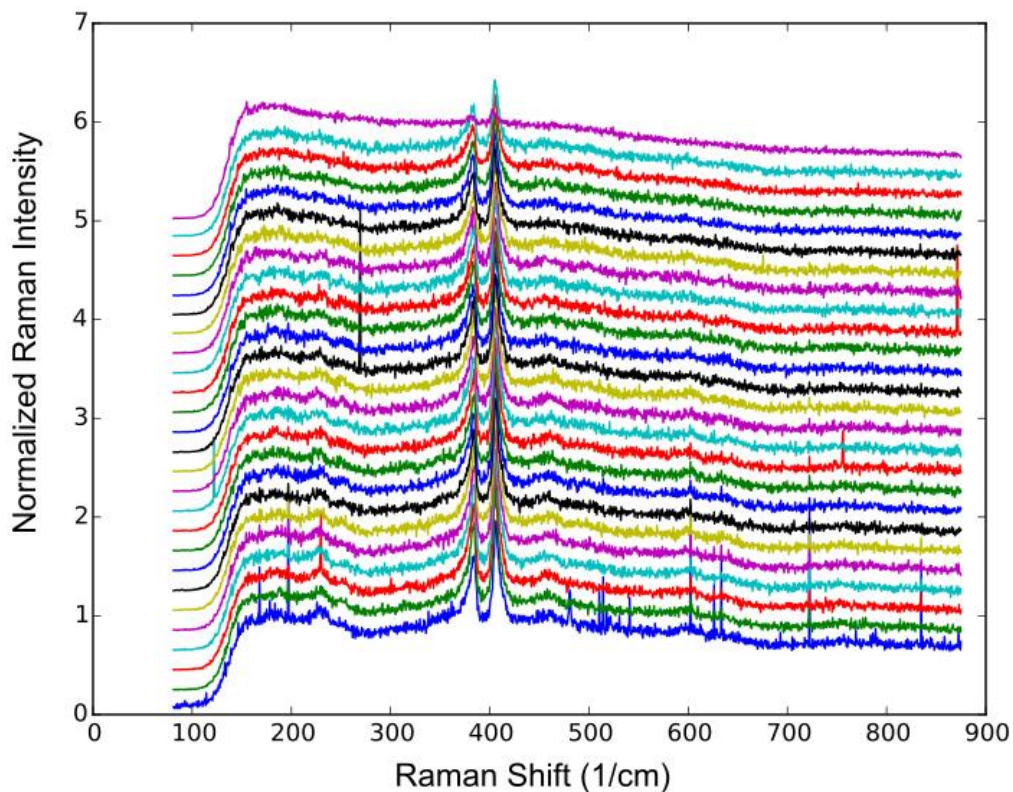
Figure SI 1.3: Raman spectra with increasing laser power for second sample. The spectra were shifted vertically for visual clarity. From bottom to top, the laser powers are 0.1 mW, 1 mW, 1 mW, 1 mW, 1 mW, 1 mW, 1.6 mW, 1.6 mW, 1.6 mW, 1.6 mW, 2 mW, 2 mW, 2 mW, 2.6 mW, 2.6 mW, 2.6 mW, 2.6 mW, 3.2 mW, 3.2 mW, 3.2 mW, 5.1 mW, 5.1 mW, 5.1 mW, 5.1 mW, 5.1 mW, and 12.5 mW. From bottom to top, the exposure times were 4000 s, 400 s, 400 s, 400 s, 400 s, 400 s, 252 s, 252 s, 252 s, 252 s, 200 s, 200 s, 200 s, 159 s, 159 s, 159 s, 159 s, 126 s, 126 s, 126 s, 126 s, 80 s, 100 s, 100 s, 100 s, 100 s, and 60 s.
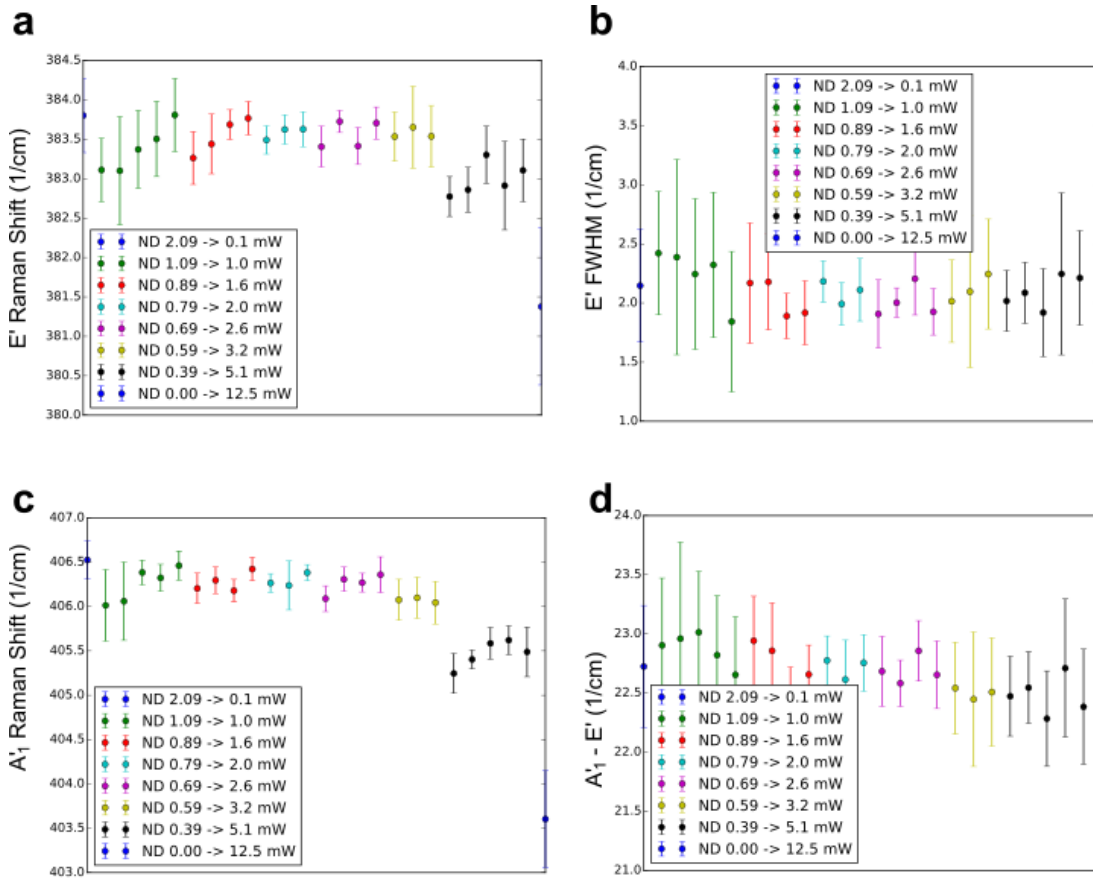
**Figure SI 1.4: Peak fits at several laser powers.** The spectra in Figure SI 1.3 were fit and peak stats were extracted. a) Location of the E' peak. b) FWHM of the E' peak. c) Location of the A'$_1$ peak. d) Separation between the E' and A'$_1$ peaks.

Section 2: Raman maps of additional MoS$_2$ flakes.

Raman maps were taken for two flakes in addition to Figure 2. Data from these flakes are

included in Figure 4.
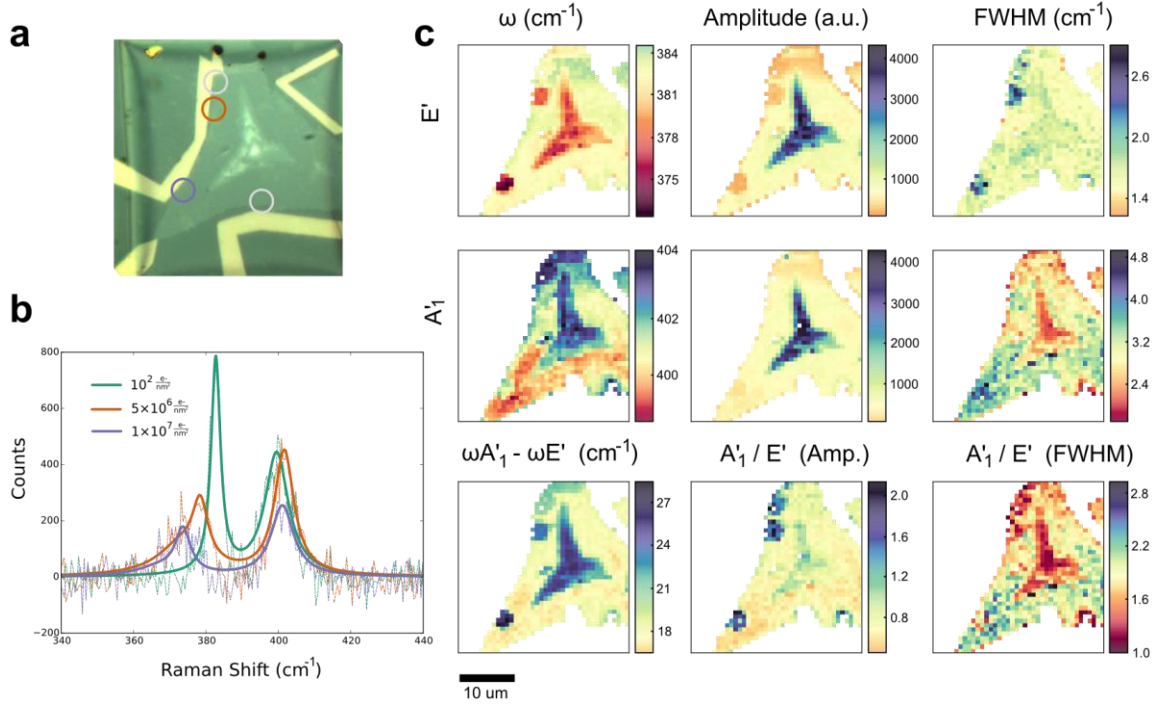
**Figure SI 2.1. Raman mapping of MoS$_2$ device showing the effects of irradiation on the E'
and A'$_1$ Raman modes.** a) Optical image of a MoS$_2$ flake on top of a SiN$_x$ window. Four circles
outline the electron-irradiated regions with doses (counter-clockwise from top left, in electrons
nm^{-2}): 1×10^6, 5×10^6, 1×10^7, 5×10^7. b) Series of corresponding Raman spectra (dotted lines) and
Lorentzian fits (solid lines) for the low dose region (green), for 5×10^6 electrons nm^{-2} (orange),
and for 1×10^7 electrons nm^{-2} (purple). The Raman peaks were not visible on the SiN$_x$ background
for a dose of 5×10^7 electrons nm^{-2}. c) (i-vi) Spatial maps of the peak shift, amplitude, and full
width at half maximum (FWHM) of the E' and A'$_1$ modes, respectively, across the device
surface. (vii-ix) Spatial maps of the E' and A'$_1$ peak separation, ratio of peak amplitudes, and
ratio of peak FWHMs. All scale bars are 10 µm.
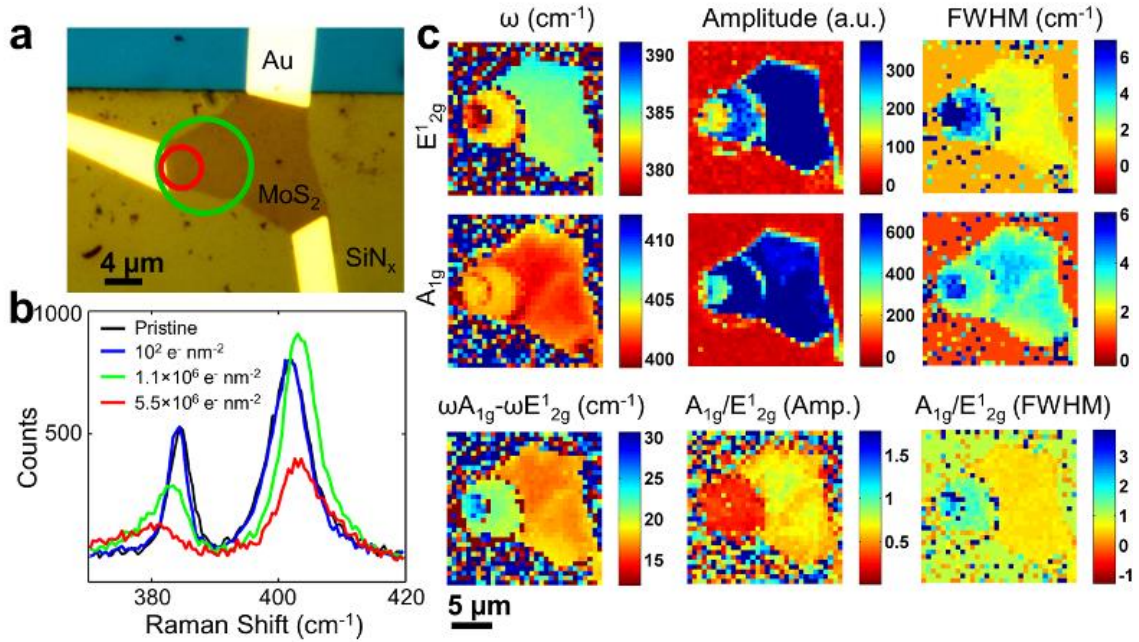
Figure SI 2.2. Raman mapping of MoS$_2$ device showing the effects of irradiation on the E$_{2g}^1$ and A$_{1g}$ Raman modes. a) Optical image of the MoS$_2$ flake transferred onto SiN$_x$, contacted by Au electrodes, and electron beam irradiated *in situ* for 20 minutes with a current density 9×10^2 electrons nm^{-2} s^{-1} (total dose 1.1×10^6 electrons nm^{-2}, green circle) and for an additional 20 minutes with 3.7×10^3 electrons nm^{-2} s^{-1} (total dose 5.5×10^6 electrons nm^{-2}, red circle). The whole sample was exposed to a small dose during the positioning procedure, estimated at less than 10^3 electrons nm^{-2}. b) Series of corresponding Raman spectra for MoS$_2$ for non-irradiated (pristine) device (black curve) and for the device in a) irradiated with dose 1 (green curve) and dose 2 (red curve). c) The first and second rows indicate the spatial map of the peak shift, amplitude, and full width at half maximum (FWHM) of the E' and A'$_1$ modes, respectively, across the device surface. The bottom row shows the spatial map of the difference and ratios in peak shifts between the A'$_1$ and E' modes across the device surface.

Section 3: Calculating Sulfur vacancy concentration from electron dose: The sputtering cross-section.

Let's take N to be our number of unit cells in an area (initially N_o), I to be the electron current density, t to be the exposure time, σ is the sputtering cross-section, D be the electron dose. Under an electron current, we can turn the sputtering cross-section into a sputtering rate by:

$$dW = I\sigma dN$$

If we assume monosulfur-vacancy formation dominates over any other defect type, we can model monosulfur-vacancy formation as random events in the following order:

1. All unit cells start with 2 Sulfur atoms. Unit cells with two Sulfur atoms will lose have the exit-side atom sputtered. We get:

$$N'_{both\_full} = -dW_{both\_full} = -N_{both\_full}I\sigma$$

where N_{both_full}' is the time derivative of the number of full unit cells, so,

$$N_{both\_full} = N_o e^{-I\sigma t} = N_o e^{-\sigma D}$$

where No is the number of unit cells.

2. Unit cells with only the entrance-side (top) Sulfur atom can have that atom pushed to the bottom. We assume the same cross-section for each of these processes[1]:

$$N'_{top} = dW_{both\_full} - dW_{top}$$

so,

$$N_{top} = N_o \sigma D e^{-\sigma D}$$

3. Unit cells with only the exit-side (bottom) Sulfur atom can have that atom sputtered. We again assume the same cross-section:

$$N'_{bottom} = dW_{top} - dW_{bottom}$$

so,

$$N_{bottom} = \frac{1}{2} N_o \sigma^2 D^2 e^{-\sigma D}$$

4. This will leave the unit cell with zero S atoms:

$$N'_{empty} = dW_{bottom}$$

so,

$$N_{empty} = N_o[1 - (1 + \sigma D + \frac{1}{2} \sigma^2 D^2)e^{-\sigma D}]$$
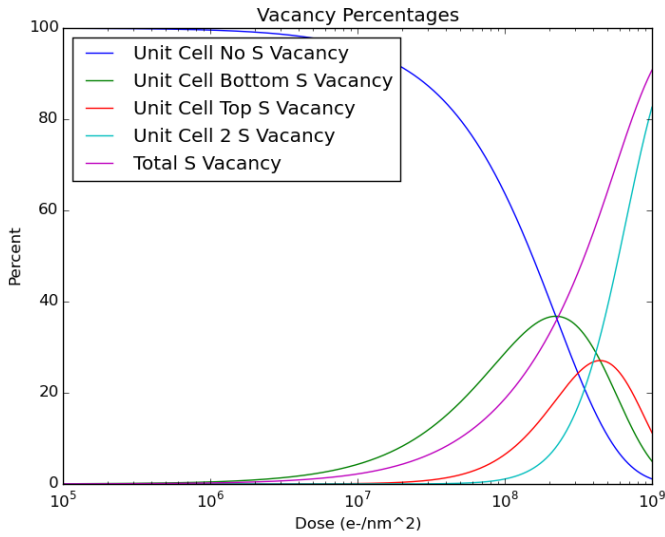
From this, the total Sulfur vacancy fraction is just

$$V_S = \frac{N_{top} + N_{bottom} + 2N_{empty}}{2N_o}$$

$$V_S = 1 - (1 + \frac{1}{2}\sigma D + \frac{1}{4}\sigma^2 D^2)e^{-\sigma D} \qquad \text{(Eq. SI 3.1)}$$

And, also useful, the fraction of unit cells with defects is just

$$Defect\ Percentage = 1 - e^{-\sigma D}$$

We can plot each term as a function of dose with $\sigma = 45$ barn:

Figure SI 3.1. S vacancy percentage as a function of dose.

Note that we expect this approximation to be valid only when monosulfur vacancies dominate (so a dose $< 2 \times 10^7$ e-/nm^2).

Section 4: Kinematic Diffraction Intensities of MoS$_2$ as a function of vacancy percentage.

The unit vectors of monolayer MoS$_2$ are

$$\boldsymbol{R_1} = a(1,0,0)$$

$$\boldsymbol{R_2} = a(\frac{1}{2}, \frac{\sqrt{3}}{2}, 0)$$

with corresponding reciprocal lattice vectors

$$\boldsymbol{K_1} = \frac{4\pi}{a\sqrt{3}}(\frac{\sqrt{3}}{2}, -\frac{1}{2}, 0)$$

$$K_2 = \frac{4\pi}{a\sqrt{3}}(0,1,0)$$

The distance between the Mo and S atoms is

$$\boldsymbol{\delta}_{+/-} = (0, \cos\theta_B, \pm\sin\theta_B)$$

$$d\cos\theta_B = \frac{a}{\sqrt{3}}$$

Where $a = 3.16$ Å, $d = 2.40$ Å, and $\theta_B = 40.6°$.[2]

The Fourier sum of an M1xM2 unit cells crystal is

$$F(\boldsymbol{q}) = \sum_{m=1}^{M_1}\sum_{p=1}^{M_2}\sum_{k=1}^{3} f_k e^{-i(\boldsymbol{k}-\boldsymbol{k}_o)\cdot(\boldsymbol{r}_g+\boldsymbol{r}_k)}$$

Because we are working with monolayer MoS2, we use the kinematic approximation. For pristine MoS2, we get

$$F(\boldsymbol{q}) = \left(f_{Mo} e^{\frac{2\pi}{3}i(2k+h)} + 2f_S \right) G(q)$$

where for small angle scattering the lattice amplitude $G(q) \propto M_1 M_2 = N$, the number of unit cells.

To consider defects, we subtract D Sulfur scatterers from the pristine Fourier sum

$$F(\boldsymbol{q}) = F_{pristine} - \sum_{n=1}^{D} f_S\, e^{-i(\boldsymbol{k}-\boldsymbol{k}_o)\cdot\boldsymbol{r}_n}$$

If we only consider **q**'s in the $[1\bar{1}00]$ family of diffraction spots, the dot product in the exponential is just a lattice vector dotted with a reciprocal lattice vector, so the sum reduces to

$$F\left(\boldsymbol{q}_{[1\bar{1}00]}\right) = F_{pristine} - Df_S$$

The diffraction intensity is proportional to $|F|^2$, so solving, normalizing to N^2, and using the

sulfur vacancy fraction $V_S = \frac{D}{2N}$ we get

$$\frac{I(q_{[1\bar{1}00]})}{N^2} = f_{Mo}{}^2 + 4f_S{}^2(1 - V_S)^2 - 2f_{Mo}f_S(1 - V_S) \qquad \text{(Eq. SI 4.1)}$$

The atomic scattering amplitudes used in this work were obtained from the electron-neutral-atom

scattering cross-sections in the International Tables for Crystallography Vol. C, Section 4.3.[3] For

the [1$\bar{1}$00] family, the atomic scattering amplitudes were $f_S = 3.16$ and $f_{Mo} = 5.65$.

Of course, many types of defects will reduce the intensities of the diffraction spots. We

consider the correlation between sputtering cross-section measured with EDS and the cross-

section measured using the diffraction intensities to be support for our monosulur vacancy

assumption, but not a proof of its validity.

## Section 5: Raman modes unaffected by deposition of amorphous carbon layer.
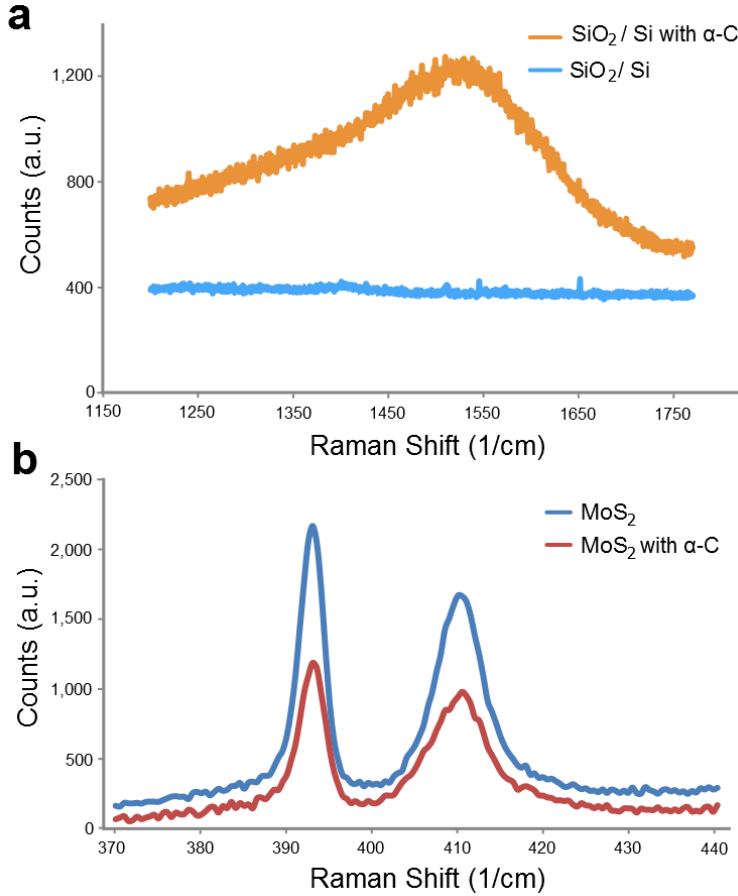
Figure SI 5.1. **α-Carbon Deposition does not affect frequencies of E' and A'$_1$ modes** It is well known that irradiation in a TEM can lead to build-up of carbon surface contaminates. To investigate the effects of carbon contaminates on the MoS2 Raman signal, we deposited a thin amorphous Carbon (α-C) layer (~5 nm) on our samples using a very low energy sputtering. We took several Raman spectra of MoS2 flakes, on SiO$_2$, before and after additional α-C layer deposition. Each Raman spectra was taken with an excitation wavelength of 532 nm for 60 seconds, with an average power of 100 mW. (a) Raman spectra of SiO$_2$/Si substrate with and without α-C. These spectra show the presence of α-C after deposition. (b) The average of MoS$_2$ Raman spectra of different flakes. We observe negligible frequency changes of the Raman modes (< 0.1 cm^{-1}) and changes in the relative intensity of the peaks, confirming that the variations described in Fig 2 and 3 (Main text) are not due to carbon contamination. A slight reduction in

the MoS2 amplitude is expected due to the 5 nm Carbon layer absorbing part of the Raman signal.

The effect of membrane charging is excluded from the possible factors of raman shift, as we observe that any charging of the membrane due to the electron beam is lost when the sample is exposed to air, by measuring continuously the conductivity of a sample going from ambient conditions to vacuum and then back.

## Section 6: DFT calculations of phonon frequency shifts.
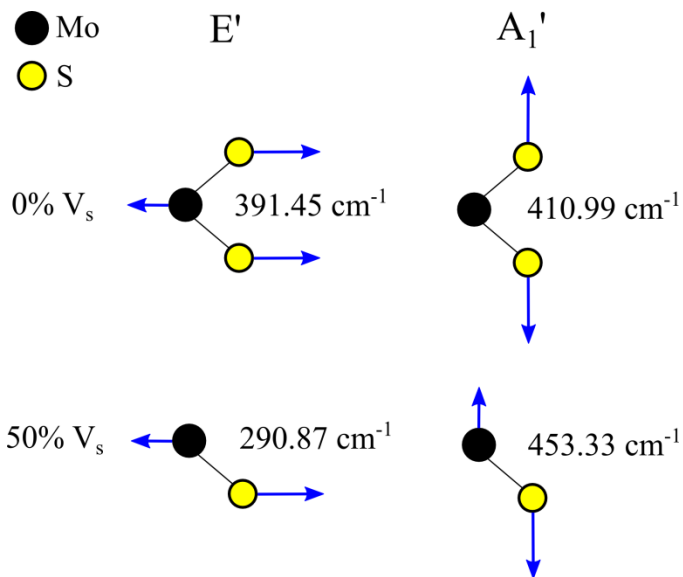
Figure SI 6.1. Calculated phonon frequencies of E' and A'$_1$ modes in monolayer MoS$_2$ with 0% and 50% monosulfur vacancy (V$_S$). The blue arrows represent the phonon vibrations. For E' mode, it corresponds to opposite in-plane vibrations of Mo and S atoms (i.e., in-plane vibrations of two Mo-S bonds) in the pristine system (0% V$_S$). In the case of 50% V$_S$, the removal of the top S atom leads to vibration of only one Mo-S bond, thus significantly weaker restoring

force constant and lower phonon frequency. The frequency of E' mode is decreased by ~ 100.6 cm^{-1} from 0% to 50% V_S. On the other hand, for A'$_1$ mode, the center Mo atom is static for the pristine system while the removal of the top S atom results in the involvement of the Mo atom into the vibration (i.e., the direct out-of-plane vibration of the Mo-S bond), hence mildly weaker restoring force constant and higher phonon frequency largely due to the reduced total mass. The frequency of A'$_1$ mode is increased by ~ 42.3 cm^{-1} from 0% to 50% V_S. Simply speaking, the force constant $K = m\omega^2$. For 0% V_S, $m = m_{Mo} + 2m_S$; for 50% V_S, $m = m_{Mo} + m_S$, where $m_{Mo} = 96u$ and $m_S = 32u$ (thus $m_{Mo} = 3m_S$). So from 0% to 50% V_S, the total mass is reduced by 20%. Based on the total mass and computed frequencies, we can infer that from 0% to 50% V_S, the restoring force constant of E' mode is reduced by ~55.8%, while the restoring force constant of A'$_1$ mode is only reduced by ~2.7%.

## Section 7: Electronic band structure of defective MoS$_2$.
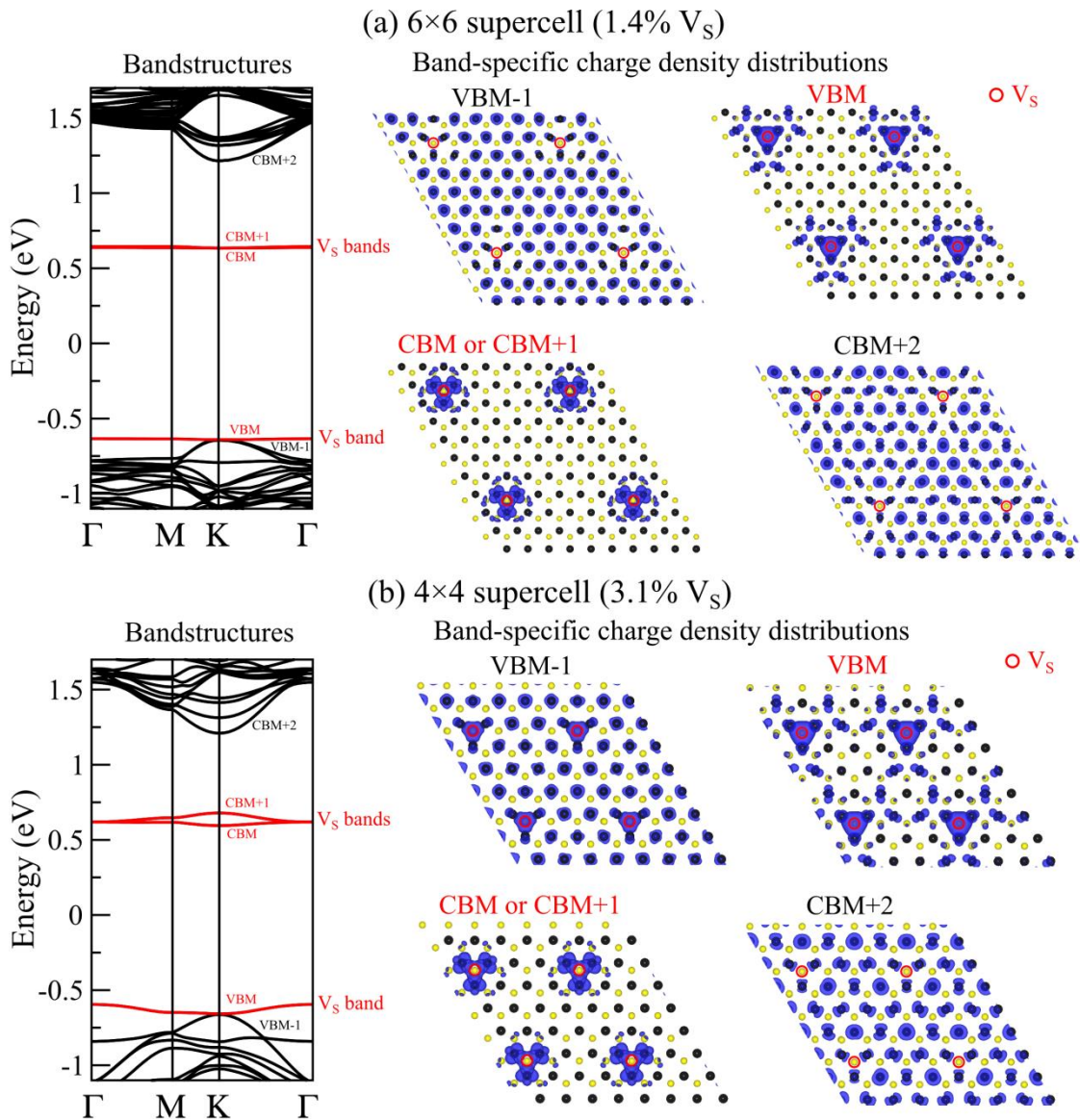
Figure SI 7.1. Electronic bandstructures and band-specific charge density distributions of 6×6 supercell and 4×4 supercell with a monosulfur vacancy (V_S). In the bandstructures, VBM (CBM) stands for valence band maximum (conduction band minimum), and V_S related bands are highlighted in red color. The Fermi level is set at 0 eV. In the charge distribution plots, black (yellow) balls correspond to Mo (S) atoms, monosulfur vacancy sites are indicated by red circles, and the isosurfaces of charge distributions are shown in blue color. Clearly, VBM-1 and CBM+2 (in black) correspond to band edges of pristine monolayer MoS_2, where their charge densities are delocalized with almost uniform distributions across the plane. In stark contrast, the charge

densities of in-gap bands induced by S vacancies (VBM, CBM, CBM+1, in red) are localized around S vacancy sites, and thus these bands are nearly dispersionless.

Section 8:Imaging during irradiation and after exposure to atmosphere.

In order check that holes in the samples are not formed during irradiation at doses used in the manuscript, we imaged suspended MoS_2 during irradiation (Figure SI 8.1). Monolayer MoS_2 flakes were transferred onto a holey-carbon TEM grid. A JEOL 2010F was used operated at 200 keV. During imaging, the beam was spread over ~112 nm diameter with a beam current density of ~7.2×10^5 e- nm^{-2} s^{-1} for 180 seconds for a total dose of 1.3×10^8 e- nm^{-2}. The lattice was intact after this dose. The sample was removed from the TEM for 10 minutes, exposing the damaged sample to atmosphere. The sample was then loaded back into the TEM, and the lattice in the damaged region was still intact. Therefore, the observed Raman shifts are not due to nanometer-sized holes in the sample. Also, the lack of unit cell sized defects suggests that we are still our defects are mainly mono[1] and line[4] vacancies.
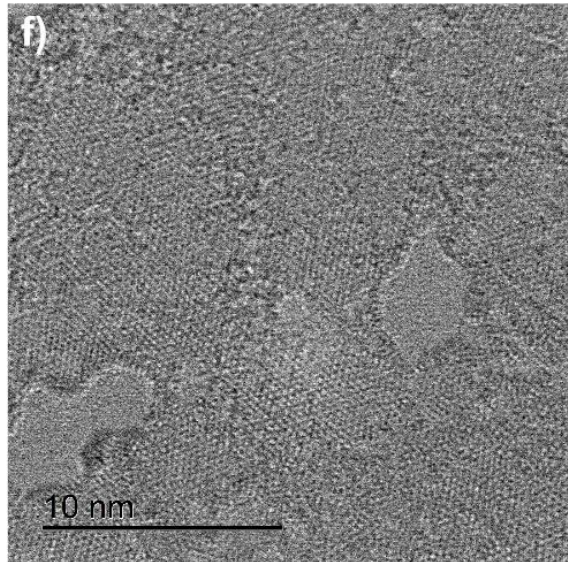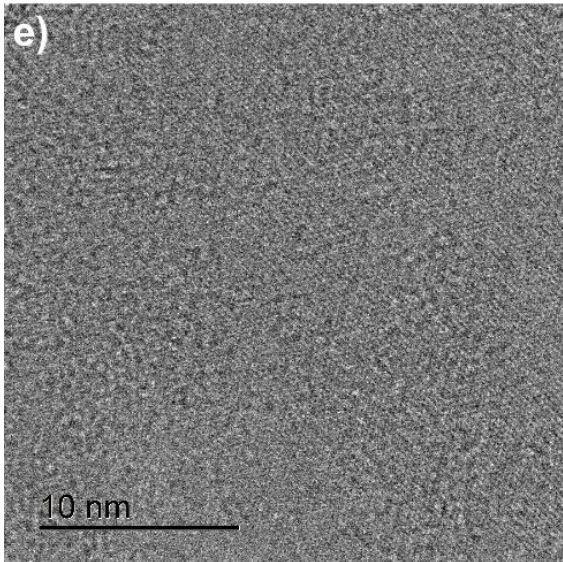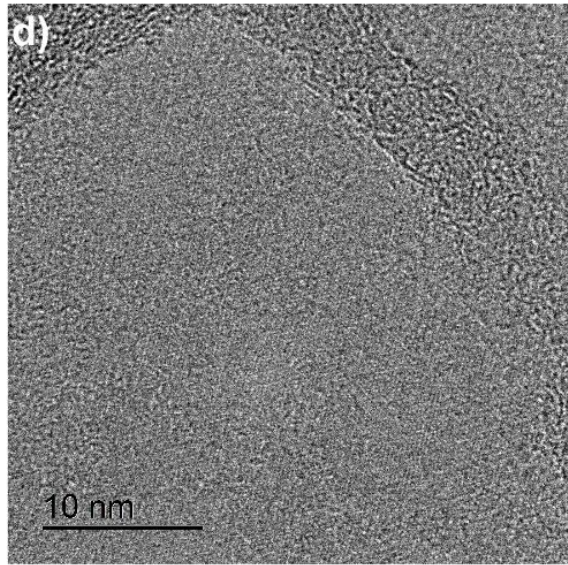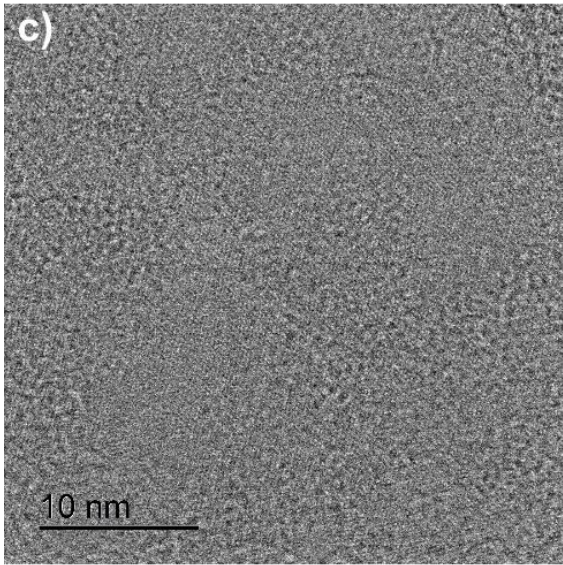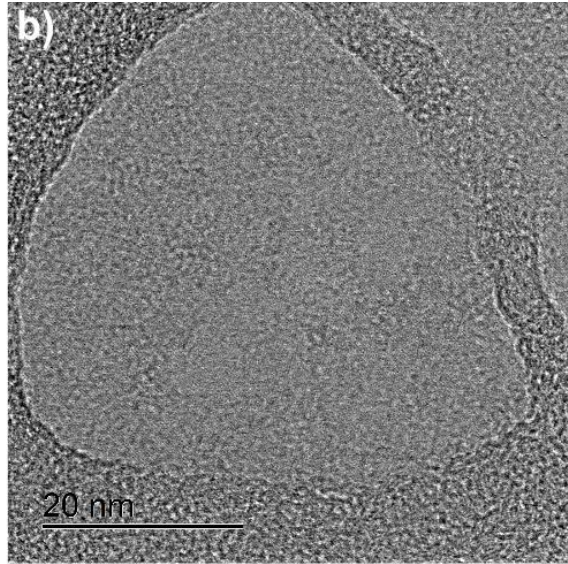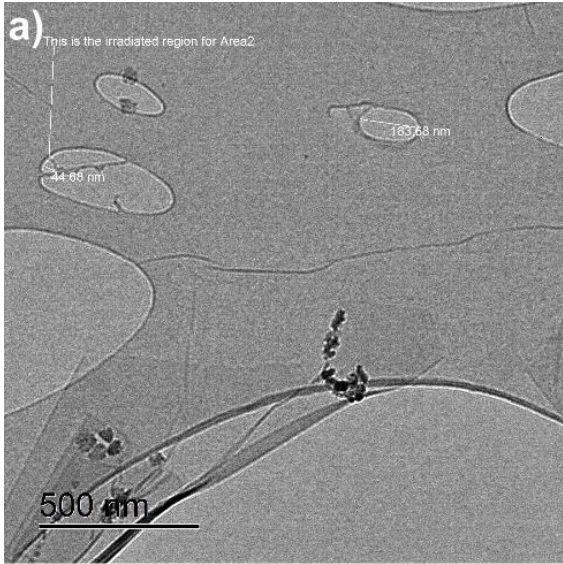
Figure SI 8.1. TEM images during and after irradiation and removal from TEM. a) HRTEM image of the area to be irradiated, indicated by the white line. b) Image of irradiated area after beam was spread over ~112 nm diameter with a beam current density of ~7.2×10^5 e- nm^{-2} s^{-1} for 180 seconds for a total dose of 1.3×10^8 e- nm^{-2}. There are no large holes seen in the lattice. c) Image of the lattice during irradiation. d) Image of the area from b) after the sample was removed from the TEM for 10 minutes. e) Image after 10 minutes in atmosphere. The lattice is still intact and no holes were observed. f) Further imaging/irradiation caused the formation of nanometer-sized holes.

Section 9: DFT calculations of effects of O substitutional impurities and line defects on phonon frequency shifts.

As oxygen atoms may substitute the S vacancy sites during Raman measurements, we have performed additional simulations to model how O substitutional impurities would affect the Raman peaks, using a 4×4 supercell with the S vacancy site substituted with the O atom. Our calculations indicate that compared to the defect-free system, the single S-vacancy system (i.e., without the O substitution) shows that the E' peak is downshifted by 4.75 cm^{-1}, while the A'$_1$ peak is upshifted by 0.47 cm^{-1}. In contrast, with the O substitution, the E' peak is downshifted by 3.34 cm^{-1}, while the A'$_1$ peak is upshifted by 1.18 cm^{-1}. These differences can be understood as follows: In general, the O substitution partially restores the bonding, so the E' peak is not downshifted as much (by ~30%), but still notably downshifted. The A'$_1$ peak also exhibits a slight upshift upon O substitution. Clearly, the O substitution cannot fully restore the sulfur deficient system, and if there is an O atom in the position of an S atom, it could still be detected as a vacancy from the Raman peak shifts.

Table SI 9.1. Calculated frequency shifts of E' and A'$_1$ modes for different defect patterns in the 4×4 MoS$_2$ supercell. The negative (positive) values indicate frequency downshifts (upshifts) of a Raman mode, compared to the pristine system.

Defect pattern	E' mode frequency shift (cm^{-1})	A'$_1$ mode frequency shift (cm^{-1})
two separated S vacancies	-7.90	0.75
two neighboring S vacancies	-8.10	-1.02
four S vacancies forming a line defect	-14.22	-1.37

1.   Komsa, H.-P.; Kotakoski, J.; Kurasch, S.; Lehtinen, O.; Kaiser, U.; Krasheninnikov, A. V. Two-Dimensional Transition Metal Dichalcogenides under Electron Irradiation: Defect Production and Doping. *Phys. Rev. Lett.* **2012**, *109*, 35503.

2.   Ridolfi, E.; Le, D.; Rahman, T. S.; Mucciolo, E. R.; Lewenkopf, C. H. A Tight-Binding Model for MoS 2 Monolayers. *J. Phys. Condens. Matter* **2015**, *27*, 365501.

3.   Colliex, C.; Cowley, J. M.; Dudarev, S. L.; Fink, M.; Gjønnes, J.; Hilderbrandt, R.; Howie, A.; Lynch, D. F.; Peng, L. M.; Ren, G.; Ross, A. W.; Smith Jr, V. H.; Spence, J. C. H.; Steeds, J. W.; Wang, J.; Whelan, M. J.; Zvyagin, B. B. International Tables for Crystallography Vol. C. In; 2006; pp. 259–429.

4.   Komsa, H.-P.; Kurasch, S.; Lehtinen, O.; Kaiser, U.; Krasheninnikov, A. V. From Point to Extended Defects in Two-Dimensional MoS2: Evolution of Atomic Structure under Electron Irradiation. *Phys. Rev. B* **2013**, *88*, 35301.